

Colors of Dynamically Associated Asteroid Pairs

Nicholas A. Moskovitz^a

^a*Carnegie Institution of Washington, Department of Terrestrial Magnetism, 5241
Broad Branch Road, Washington, DC 20008 (U.S.A)*

Copyright © 2012 Nicholas A. Moskovitz

Number of pages: 22

Number of tables: 5

Number of figures: 7

Proposed Running Head:

Colors of asteroid pairs

Please send Editorial Correspondence to:

Nicholas A. Moskovitz

Department of Terrestrial Magnetism

Carnegie Institution of Washington

5241 Broad Branch Road

Washington, DC 20008, USA.

Email: nmoskovitz@dtm.ciw.edu

Phone: (202) 478-8862

1 **ABSTRACT**

2 Recent dynamical studies have identified pairs of asteroids that reside in nearly
3 identical heliocentric orbits. Possible formation scenarios for these systems in-
4 clude dissociation of binary asteroids, collisional disruption of a single parent
5 body, or spin-up and rotational fission of a rubble-pile. Aside from detailed
6 dynamical analyses and measurement of rotational light curves, little work has
7 been done to investigate the colors or spectra of these unusual objects. A pho-
8 tometric and spectroscopic survey was conducted to determine the reflectance
9 properties of asteroid pairs. New observations were obtained for a total of
10 34 individual asteroids. Additional photometric measurements were retrieved
11 from the Sloan Digital Sky Survey Moving Object Catalog. Colors or spectra
12 for a total of 42 pair components are presented here. The main findings of
13 this work are: (1) the components in the observed pair systems have the same
14 colors within the uncertainties of this survey, and (2) the color distribution of
15 asteroid pairs appears indistinguishable from that of all Main Belt asteroids.
16 These findings support a scenario of pair formation from a common progen-
17 itor and suggest that pair formation is likely a compositionally independent
18 process. In agreement with previous studies, this is most consistent with an
19 origin via binary disruption and/or rotational fission.

20 *Keywords:* Asteroids; Photometry; Spectroscopy

21 1 Introduction

22 Analyses of osculating orbital elements of Main Belt asteroids have revealed
23 over 80 pairs of asteroids that reside in nearly identical heliocentric orbits
24 (Vokrouhlický and Nesvorný, 2008; Pravec and Vokrouhlický, 2009; Rožek et
25 al., 2011). These objects are distinct from binary asteroids as they are not on
26 bound orbits around a common center of mass, and it is unlikely that their
27 proximity is due to random fluctuations of asteroid densities in orbital element
28 space. Backwards integration of these pairs’ heliocentric orbits suggests they
29 may have separated recently into an unbound state, in some cases much less
30 than a Myr ago (Vokrouhlický and Nesvorný, 2009; Vokrouhlický, 2009; Pravec
31 et al., 2010; Vokrouhlický et al., 2011; Duddy et al., 2012). As such these are
32 interesting objects for studying phenomena, such as space weathering and
33 radiation pressure forces, that are relevant to the ongoing dynamical, physical
34 and chemical evolution of Main Belt asteroids.

35 The components of known pairs are typically a few km in size and consist of a
36 primary and a secondary (respectively defined as the larger and smaller com-
37 ponents based on measured absolute magnitudes). One formation scenario for
38 these systems (Scheeres, 2007; Pravec et al., 2010) involves parent asteroids
39 that were spun up to a critical frequency by the YORP effect, i.e. a change in
40 angular momentum due to anisotropic emission of thermal photons (Rubin-
41 cam, 2000; Bottke et al., 2006). At this critical frequency the parent would
42 fission into a proto-binary system and eventually disrupt under its own in-
43 ternal dynamics to form an unbound asteroid pair (Jacobson and Scheeres,
44 2011). The estimated size ratios and observed rotational properties of known
45 pair systems are consistent with a formation scenario via rotational fission
46 (Pravec et al., 2010). Progressive mass shedding due to YORP spin-up and

47 accretion of a dynamically unstable proto-satellite offers a similar pathway
48 to pair formation (Walsh et al., 2008). The close spectral similarity between
49 components in one pair system (Duddy et al., 2012) and the photometric sim-
50 ilarity between components in another (Willman et al., 2010) support these
51 scenarios.

52 Though a fission origin is consistent with the size ratios and rotation proper-
53 ties for a large number of pairs (Pravec et al., 2010), collisions provide another
54 possible formation mechanism that may explain a subset of systems. In this
55 scenario a catastrophic collision would produce a distribution of fragments,
56 of which only the largest two are observed as an associated pair. Collisions
57 between small bodies can result in compositionally complex outcomes (e.g.
58 Leinhardt et al., 2009), but it is unclear how collisional formation would af-
59 fect the relative colors and/or spectra of the km-scale objects found in pair
60 systems. Aside from any spectroscopic or photometric implications, hydrody-
61 namic simulations of impact events make predictions about the resulting or-
62 bital properties and size ratios of collisional fragments (Nesvorný et al., 2006;
63 Durda et al., 2007). Unfortunately, due to incompleteness for sub-km bodies
64 in the Main Belt, it is currently not possible to fully test these predictions
65 (Vokrouhlický and Nesvorný, 2008).

66 A final formation mechanism involves the dynamical dissociation of bound
67 binary systems. Perhaps the best evidence for ongoing pair formation via
68 binary disruption comes from the system of asteroids associated with 3749
69 Balam. Adaptive optics and light curve observations (Merline et al., 2002;
70 Marchis et al., 2008a,b; Polishook et al., 2011) have shown that Balam has
71 two bound satellites, making it a rare triple system. One of its two satellites is
72 on a highly eccentric orbit ($e \sim 0.9$), while the other orbits at a distance of only

73 20 km (Balam itself is about 5-10 km in size). In addition, this triple system
74 has a dynamically associated pair, asteroid (312497) 2009 BR60. Backwards
75 numerical integrations show that the orbits of Balam and 312497 converge
76 within the past 0.5 Myr (Vokrouhlický, 2009). Numerical models suggest that
77 a cascade of fragments, like that seen in the Balam system, can result from
78 repeated rotational fission events (Scheeres and Sánchez, 2011). It seems in
79 this case that YORP fission and binary dissociation may be closely related
80 processes.

81 However, it is unclear how the compositions of asteroid pairs would reflect an
82 origin due to the dissociation of binaries. Component-resolved spectra have
83 been obtained for a very small number of bound binary systems (e.g. Pol-
84 ishook et al., 2009; Marchis et al., 2011; DeMeo et al., 2011). This is in part
85 due to the need for either adaptive optics or space based observations to
86 resolve the individual components. Available spectra suggest that the compo-
87 nents of binaries are compositionally similar, however data is scarce and more
88 information is required before generalized statements can be made.

89 In light of these various formation mechanisms, there remain several unad-
90 dressed questions regarding the formation and evolution of asteroid pairs. For
91 instance, the relationship between pairs and bound multi-component systems
92 is unclear. In addition, little is known about their compositions/taxonomic
93 types. Different formation mechanisms could affect the relative compositions
94 of pair components in different ways. However, for each of these mechanisms
95 the physics of separation should predominantly depend on the internal (rubble
96 pile) structure and density of the parent asteroid. Objects in the size range of
97 asteroid pairs are expected to be rubble piles (Pravec and Harris, 2000). It is
98 possible that a variety of formation mechanisms are responsible for the forma-

tion of the ensemble population of asteroid pairs. Reflectance spectroscopy or photometric colors may help to provide arguments regarding the mechanism of formation on a case-by-case basis.

Here we present a survey of asteroid pairs to constrain their spectro-photometric properties. The observations, data reduction and error analysis are presented in §2. This data set provides the means to investigate the relative reflectance properties of pair primaries and secondaries, and facilitates a direct comparison to the color distribution of ordinary Main Belt asteroids (§3). The results and implications of this survey are discussed in §4.

2 Observations and Data Reduction

New optical observations of 34 individual asteroids were performed. In the majority of cases *BVRI* photometric colors were measured. Visible wavelength spectra were obtained for two objects, and for one object Gunn *gri* photometry was obtained. In addition, *ugriz* photometry of 16 pair components were retrieved from the 4th release of the Sloan Digital Sky Survey Moving Object Catalog (SDSS MOC, Ivezić et al., 2001). Six of these SDSS pairs overlap with our sample. In total, data were acquired for at least one component in 30 pair systems and for both components in 12 pair systems. A previously reported pair that has since been found to be spurious was also observed (see §3.2). Targets for observation were selected from Pravec and Vokrouhlický (2009) based on observability during the scheduled observing runs. Table 1 summarizes the observing circumstances for each target.

121 2.1 Photometry

122 Photometric observations were conducted at three different facilities: with
123 IMACS at the Magellan Baade 6.5m telescope at Las Campanas Observatory
124 in Chile, with the SITe2k CCD at the DuPont 2.5m telescope also at Las
125 Campanas, and with the SNIFS instrument (Lantz et al., 2004) at the Uni-
126 versity of Hawaii 2.2m telescope on Mauna Kea. IMACS was operated using
127 the $f/2$ camera, which has a 27.5' field-of-view covered by a mosaic of eight
128 2k x 4k CCDs with plate scales of 0.2 "/pixel. The SITe2k at DuPont is a 2k x
129 2k CCD with an 8.85' field-of-view with a plate scale of 0.259 "/pixel. SNIFS
130 was operated in imaging mode with its 4k x 4k CCD covering a field-of-view
131 of approximately 9' at a plate scale of 0.137 "/pixel. Observations were per-
132 formed in February and August of 2010 with the SITe2k at DuPont, in March
133 and August of 2010 and in March of 2011 with IMACS at Magellan, and in
134 February of 2012 with SNIFS at the UH2.2m. The telescopes were operated
135 in non-sidereal tracking modes when integration times were long enough to
136 have resulted in trailing greater than the measured seeing. When using on-
137 chip calibration stars (see below) we tracked at 1/2 the non-sidereal rate of the
138 asteroid such that the asteroid and field stars shared a common point spread
139 function. When not using on-chip calibration stars tracking was performed at
140 the non-sidereal rate of the asteroid.

141 Different filter sets were used at each facility. With IMACS Bessell BVR and
142 CTIO I filters were used. The band centers of these filters are 0.44, 0.55, 0.64,
143 and 0.82 μm respectively. At the DuPont telescope, Johnson BV and Kron-
144 Cousins R_cI_c were employed. The band centers for these filters are the same as
145 the Bessell set with the exception of I_c with a center at 0.85 μm . With SNIFS
146 the Gunn gri filter set was used with band centers of 0.47, 0.62 and 0.75 μm .

147 Data retrieved from the SDSS MOC correspond to *ugriz* filters centered at
148 0.35, 0.47, 0.62, 0.75, and 0.89 μm respectively.

149 Observations were typically conducted in sequences with interspersed *V*- or
150 *r*-band measurements to monitor variability due to observing conditions or
151 rotation of the asteroid. For example, a single observing sequence would in-
152 volve taking a set of seven images with a filter order of *VBVRVIV*. In this
153 case the mean value of adjacent *V*-band magnitudes would be used to com-
154 pute the $B - V$, $V - R$ and $V - I$ colors. In some cases only single exposures
155 were taken in each band. Though this was not ideal for producing perfectly
156 calibrated photometry, the gain in observing efficiency allowed us to increase
157 our sample to a statistically significant size. Any errors introduced by taking
158 single exposures (for instance not being able to correct for light curve variabil-
159 ity) should be random and small since fewer than 20 minutes were typically
160 needed for single *BVRI* exposures.

161 Data reduction employed standard IRAF routines for overscan correction, bias
162 subtraction, flat fielding, and aperture photometry. Aperture radii were set to
163 minimize the photometric error of the asteroid measurement. Since, the aster-
164 oids were always fainter than or roughly equal in brightness to the calibration
165 stars, the errors introduced by background noise from the asteroid measure-
166 ment always dominated the net photometric uncertainty. Choosing an aper-
167 ture that minimized photometric noise ensured the highest quality results.
168 With median seeing around 0.65'' at Las Campanas, typical aperture radii of
169 $\sim 1 - 2''$ were employed. Background annuli were defined to have a radius of
170 4'' from the photocenter of the target and a width of 8''.

171 Photometric calibration was achieved in one of two ways. When the target
172 was in an SDSS field, up to 15 on-chip stars with solar-like colors were used

173 to calibrate the instrumental magnitude of the asteroid by determining a sin-
 174 gle photometric correction factor based on the difference between the SDSS
 175 stars' measured and catalog magnitudes. Definitions of solar colors from the
 176 SDSS website¹ and $BVRI \rightarrow ugriz$ transforms (Jester et al., 2005) were em-
 177 ployed. SDSS stars much more than two or three magnitudes brighter than
 178 the asteroid were often saturated, while those much fainter than the asteroid
 179 were not used to avoid introducing extra error into the photometric calibra-
 180 tion. This resulted in using field stars with magnitudes roughly comparable to
 181 or a few magnitudes brighter than the asteroid. When SDSS field stars were
 182 not available, Landolt standard fields were observed at a range of airmasses
 183 and at several times throughout the night to fit a photometric transform so-
 184 lution (zero point, airmass term and color term). As a test, several objects
 185 were calibrated with both techniques. In all tests the resulting photometry
 186 was consistent within 0.1 magnitudes. Apertures for calibration stars (both
 187 Landolt and SDSS) were set equal to that used for each asteroid.

188 Tables 2 and 3 summarize the results of our collected photometry. Phase
 189 corrected absolute magnitudes (H_V) are calculated for each object in Table
 190 2. Phase and distance corrections to the measured apparent magnitudes were
 191 applied using the observational data in Table 1 and the formalism of the IAU
 192 H-G system (Bowell et al., 1989). A slope parameter of 0.15 was assumed
 193 for all asteroids. No attempts were made to accurately account for the full
 194 rotational variability of the targets. Accounting for the possible range of slope
 195 parameters and light curve amplitudes suggests that the calculated absolute
 196 magnitudes are accurate to approximately ± 0.5 . In general these absolute
 197 magnitudes are several tenths higher than those reported by the Minor Planet
 198 Center and JPL Horizons. This is a well known bias in these catalogs that

¹ <http://www.sdss.org/dr4/algorithms/sdssUBVRITransform.html>

199 may be attributed to the use of open, unfiltered images for the majority of
200 reported measurements (Jurić et al., 2002).

201 Tables 2 and 3 make several notes about individual objects. It is noted when
202 an object was observed on several occasions, either with different instruments
203 or by SDSS. It is noted when multiple *BVRI* or *gri* sequences were obtained
204 for a given object within a night. The magnitudes and colors for objects with
205 multiple sequences represent mean values weighted by the signal-to-noise ra-
206 tios of the individual observations. A full listing of all *V*-band magnitudes
207 from individual exposures are included in the online Supplementary Data. The
208 error bars in Tables 2 and 3 are addressed in §2.3. Finally, it is noted when
209 SDSS field stars were used for photometric calibration. All other observations
210 were calibrated with Landolt standards.

211 The data for one complete pair (asteroids 17288 and 203489) are shown in
212 Figure 1. These data have been solar-corrected assuming solar colors (from
213 the SDSS website) of $B - V = 0.65$, $V - R_C = 0.36$, and $R_C - I_C = 0.32$,
214 and thus provide coarsely sampled reflectance spectra of these asteroids. All
215 subsequent presentations of our data will show solar-corrected values. This is
216 not the case for the photometry in Tables 2 and 3.

217 2.2 Spectroscopy

218 In two cases the targets were sufficiently bright that visible wavelength (0.45-
219 $0.82\ \mu\text{m}$) spectra were obtained with IMACS operating in its long-slit, low-
220 resolution mode with a 200 lines/mm grism. These settings produce a single-
221 order spectrum that spans two of the IMACS 2k x 4k chips at a dispersion
222 of approximately $2\ \text{\AA}/\text{pixel}$ with a small gap in wavelength coverage around

223 0.6 μm . A blocking filter with a cutoff at 0.455 μm was employed to prevent
224 contamination from higher orders. The observing circumstances for the two
225 spectroscopic targets are summarized in Table 4.

226 Reduction of these spectra employed standard IRAF and IDL routines to
227 overscan correct, bias subtract, flatten, extract, dispersion correct, combine,
228 normalize and re-bin the data. Solar analog stars were observed close in time
229 and pointing location to the asteroids (Table 4). In the case of asteroid 10123
230 and its analog SA104-335, both spectra were obtained within a span of 30
231 minutes and at a difference in airmass of 0.04. For asteroid 99052 and its analog
232 HD127913, the two spectra were obtained within 40 minutes of one another
233 and at a difference in airmass of 0.03. The angular separations of the asteroids
234 and their respective analogs were less than 20° . The extracted asteroid spectra
235 were divided by their respective analogs and normalized to produce relative
236 reflectance spectra. Combined He, Ne and Ar arc lamp spectra were obtained
237 immediately after each target to provide pointing-specific dispersion solutions.

238 Figure 2 presents both a spectrum and photometry for asteroid 99052. These
239 two techniques produce similar spectral profiles with only slight differences in
240 slope. Light curve variability was not accounted for in the photometric data
241 and thus could be the cause of its slightly redder slope, however the light
242 curve period of 99052 is currently unknown. Another factor could be that
243 the spectroscopic calibration star HD127913 (Table 4) is not a perfect solar
244 analog.

245 The observed spectra provide the means for more accurate taxonomic clas-
246 sification than can be achieved with broad band photometry. We assign a
247 taxonomic type to each of the observed spectra by conducting a chi-squared
248 minimization search through the mean spectral values for each of the SMASS

249 taxa (Bus and Binzel, 2002). The best-fit taxa are given in Table 4.

250 2.3 Consistency Checks and Error Analysis

251 Our data set provides several methods for checking the quality and repeatabil-
252 ity of the observations. The most obvious check is to compare intra- and inter-
253 night observations of the same object. Repeat intra-night observations of the
254 same object generally resulted in less than 0.05 magnitude variability in colors.
255 As such the colors in Tables 2 and 3 represent weighted means of all measured
256 colors within a night. Asteroid 17288 was observed with IMACS/Magellan
257 and the SITe2k/DuPont on two separate nights. The colors from these obser-
258 vations are very similar (Fig. 1). Asteroid 143662 was observed on two separate
259 nights with the SITe2k/DuPont. The photometry for this object shows some
260 inconsistency with colors differing up to 0.07 magnitudes between nights but
261 are still consistent within the errors (Table 2).

262 Asteroid 195479 was observed with IMACS/Magellan and the SITe2k/DuPont
263 on two separate nights. The photometry roughly agrees between these sets of
264 observations, however the $V - R$ colors differ by 0.08 magnitudes (Table 2).
265 This could be due to the use of different calibration methods, i.e. using SDSS
266 field stars versus Landolt standards. Another possible cause is the lack of
267 any light curve corrections to the IMACS data. In the case of the IMACS
268 observations, a single $BVRI$ sequence was obtained, taking less than 25 min-
269 utes to complete. With the DuPont data, light curve corrections were possible
270 and applied because the brightness of 195479 monotonically increased by two-
271 tenths of a magnitude over the 2.5 hours necessary to complete the exposure
272 sequence. This variability was much larger than the photometric errors and
273 thus a strong indication of light curve variability. Regardless of the cause of

274 this offset in $V - R$ color, this is the largest discrepancy amongst any of our
275 repeat observations.

276 Another consistency check is to compare our data to that of objects included
277 in the SDSS MOC. This overlap includes 6 objects (Table 3) and in all cases
278 the difference in colors is no more than 0.06 magnitudes. For 4 of these 6 the
279 color differences are less than 0.02 magnitudes. Figure 1 shows the close match
280 between SDSS photometry and new observations for two asteroids. The close
281 match between our spectroscopic and photometric observations of 99052 (Fig.
282 2) provides a final confirmation of data quality.

283 Based on the general consistency of these data, a *conservative* estimate to the
284 systematic uncertainties in the photometric calibration is ± 0.1 magnitudes.
285 This estimate accounts for issues of uncorrected light curve variability, non-
286 photometric observing conditions, and the use of imperfect calibration stars
287 and is unrelated to the signal-to-noise of the observations. We adopt this
288 limit as an estimate to the overall accuracy of this survey and employ it
289 in a statistical comparison of pair colors (§3). This limit to the systematic
290 uncertainties is not large enough to affect any of the following conclusions or
291 analysis.

292 The error bars reported in Table 2 merit further discussion. Due to the large
293 range of observed magnitudes (from 17.5 up to 22.5), the measurement uncer-
294 tainty on the brightest targets will be dominated by systematic errors, whereas
295 background noise dominates for the fainter targets. It is unclear where the
296 transition between these two regimes exists and, as the previous discussion
297 indicates, it is non-trivial to estimate systematic errors. Therefore the errors
298 reported here fall into one of two categories. In the case of objects observed
299 with a single $BVRI$ sequence, the errors represent the signal-to-noise of the

300 data as set by background noise levels with standard error propagation for the
 301 colors. In the case of objects observed with multiple *BVRI* sequences (as de-
 302 noted by ^c in Table 2), the uncertainty on the V-band magnitudes represents
 303 one standard deviation across all measurements. Hence, the standard devia-
 304 tions of these V-band magnitudes provide a lower limit to the light curve am-
 305 plitude of the targets even though no full rotational light curves were resolved.
 306 The best example of a partially resolved light curve was for asteroid (69142)
 307 2003 FL115, which monotonically increased in brightness from $V = 20.3$ to
 308 $V = 19.9$ across 10 exposures during the hour and a half in which it was ob-
 309 served. Hence the ± 0.19 uncertainty on the calibrated V-band magnitude for
 310 69142 in Table 2 represents the standard deviation of these 10 measurements
 311 and is likely indicative of light curve variability of the asteroid. The uncer-
 312 tainties on the colors for these multi-sequence targets represent the errors on
 313 the weighted means.

314 **3 Analysis**

315 Comparison of multi-band photometry is facilitated by assigning a single diag-
 316 nostic parameter to each set of multi-band measurements. An obvious choice
 317 for this parameter is a modification for the *BVRI* filter set of the a^* principal
 318 component color defined by Ivezić et al. (2001):

$$319 \quad a^* = 0.908 \cdot (B - V) + 0.409 \cdot (R_C - I_C) - 0.856. \quad (1)$$

320 This modification is based on the *BVRI* \rightarrow *ugriz* transform equations of Jester
 321 et al. (2005) and redefines the $B - V$ versus $R_c - I_c$ color space to maximize
 322 the separation of C- and S- complex asteroids, thus providing a means for

coarse taxonomic assignment. The utility of a^* as a tool for such taxonomic assignment is due to its strong correlation with spectral slope (Nesvorný et al., 2005). This principal component color is computed for each of the asteroids in Tables 2 and 3. The errors on a^* represent a propagation of the reported $B - V$ and $R_C - I_C$ errors through Equation (1).

3.1 Comparison of Primary and Secondary Colors

We first compare a^* colors of the primary and secondary components (Table 5, Fig. 3). The a^* colors of the components in each pair are the same within the reported error bars. Table 5 includes an assignment of taxonomic complex for each of the pairs. Only the S- and C-complexes are considered here and are distinguished by positive or negative a^* values respectively. We make no attempt to distinguish specific taxonomic types due to the coarse spectral sampling of the broad band photometric filters. In reality this rough taxonomic assignment lumps a variety of classes into each complex. Asteroids with positive a^* include the S-, D-, A-, R-, L- and V-classes, while those with negative a^* include C-, B- and X-types (Ivezić et al., 2001; Bus and Binzel, 2002).

Figure 3 presents observations for the 11 complete pairs; no SDSS or spectroscopic data are included. The components for a majority (10/11) of these pairs have the same a^* colors within the estimated ± 0.1 magnitude systematic uncertainties. The pair 69142-127502 falls outside of the limits set by the estimated uncertainties. The spectro-photometry for this pair is shown in Figure 4. The a^* values for these asteroids are 0.15 ± 0.12 and 0.04 ± 0.14 respectively. These colors are indistinguishable within the error bars, which are some of the largest reported here (Tables 2 and 3). The photometric similarity of these

348 objects is apparent in Figure 4. The large difference in their a^* colors is most
349 likely a consequence of the different filter sets and highlights the limitations of
350 comparing individual objects (as opposed to a statistical comparison) based
351 on broad band photometric measurements.

352 The pair 10123-117306 is not included in Figure 3. This is due to an incom-
353 plete *BVRI* sequence for 117306 caused by the asteroid passing over a field
354 star during the *I*-band exposure. This made it impossible to reliably calibrate
355 the photometry in that band and to calculate an a^* value. Nevertheless, the
356 spectral profiles of the asteroids in this pair, particularly the unusually red
357 slope, are very similar (Fig. 5). It is reasonable to suggest that the reflectance
358 properties of 10123-117306 would result in this pair plotting near the slope-one
359 line in Figure 3.

360 Data were also obtained for the reported pair 34380-216177 (Fig. 6). The
361 photometry for this system resulted in significantly different a^* colors for the
362 two components (Tables 2 and 3). This does not have a bearing on our results:
363 the probability of association for this pair was one of the lowest in Pravec and
364 Vokrouhlický (2009) and updated dynamical integrations failed to reveal an
365 orbital convergence within the past 2 Myr (P. Pravec, private communication,
366 April 2012). Therefore, this pair is now considered spurious and is not included
367 in the analysis here.

368 The significance of the apparent correlation between pair colors in Figure
369 3 is tested by comparing a^* colors for random asteroids selected from the
370 SDSS MOC. To perform this test a^* is calculated for a randomly selected
371 Main Belt asteroid. An a^* color is then calculated for the next closest object
372 in orbital element space as defined by the distance metric of Zappalà et al.
373 (1994). This pseudo-pair is plotted on the axes of Figure 3 and the process

374 is repeated 12 times to mimic the set of complete pair systems (including
 375 10123-117306) observed here. The number of pseudo-pairs that fall outside
 376 of the ± 0.1 region is then recorded. This Monte Carlo style selection of 12
 377 pseudo-pairs is repeated 10,000 times. This test shows that in only 1.7% of
 378 the trials do 11 out of the 12 psudeo-pairs have a^* colors within ± 0.1 of each
 379 other. In other words, 98.3% of these trials show a distribution of colors less
 380 correlated than those in Figure 3. Only 0.2% of the time do all 12 pseudo-
 381 pairs have a^* colors within ± 0.1 of each other. This would be the case if we
 382 assume that additional data of pair 69142-127502 revealed a closer match in
 383 a^* . This test suggests with greater than 98% significance that the correlation
 384 between a^* colors for asteroids pairs is not a random result. Reducing the
 385 conservative estimate for the systematic uncertainties of this survey in half
 386 to ± 0.05 increases the probability of a non-random a^* distribution to $> 99\%$,
 387 further supporting the conclusion that the components in asteroid pair systems
 388 have the same colors.

389 3.2 *Comparison of Pairs to Main Belt Asteroids*

390 The a^* colors of all 40 asteroid pairs presented here (our 30 complete pho-
 391 tometric observations plus 10 from SDSS and excluding the spurious pair
 392 34380-216177) are compared to those of Main Belt asteroids from the SDSS
 393 MOC (Fig. 7). The bi-modality in these histograms is indicative of the a^* color
 394 separation of C- and S-complex asteroids. From this figure it is clear that, by
 395 definition, an a^* color cut at 0.0 roughly segregates these two complexes (Ta-
 396 ble 5). However, we note that a^* is not meant to provide detailed taxonomy
 397 and that the assignment of a taxonomic complex to objects with error bars
 398 that straddle the 0.0 cut is somewhat arbitrary due to the the clear overlap of

399 the C- and S-complexes at these values. This ambiguity in taxonomic typing is
400 largely irrelevant to this study, but could be resolved with future spectroscopic
401 observations.

402 Both histograms in Figure 7 are influenced by observational biases. This is
403 clear in the apparent over-abundance of S-types. In fact debiased estimates
404 suggest that C-types are more numerous by a factor of more than two to one
405 in the Main Belt (Ivezić et al., 2001). For our observations, no attempts were
406 made to obtain an unbiased photometric sample of asteroid pairs. In spite
407 of these limitations, it is reasonable to suggest that to first order the biases
408 inherent to SDSS also affected our observations. We were magnitude limited
409 to those objects that could be observed on a specific date, in similar fashion
410 to detection limits inherent to the SDSS. Therefore a qualitative comparison
411 of these histograms is justified.

412 Though both histograms in Figure 7 have bi-modal distributions, it appears
413 that the C-type pairs are slightly shifted towards positive a^* colors. However,
414 this is likely a result of low number statistics and not a robust trend. A two-
415 sided Kolmogorov-Smirnov test suggests the likelihood that these distributions
416 are drawn from different parent populations is significant at only the 1.4-sigma
417 level. Hence, the colors of asteroid pairs observed in this survey are statistically
418 indistinguishable from the overall population of Main Belt asteroids.

419 4 Discussion

420 We have presented results and analysis of a spectro-photometric survey of dy-
421 namically associated asteroid pairs. A combination of new observations and
422 archival data from the SDSS MOC have provided insight on the reflectance

properties of 44 individual asteroids in 30 pair systems and one spurious pair. Data were obtained for both components in 12 pair systems. These data suggest a correlation between the colors of primary and secondary components (Fig. 3) at greater than 98% significance. We suggest this argues in favor of a common origin for these pairs.

The components in one of the observed systems, 34380-216177, have significantly different colors (Fig. 6). However, updated dynamical integrations have revealed that this is a spurious pair (P. Pravec, private communication, April 2012) and thus should not have been included in our survey. This highlights the need for future follow-up observations of other dynamically identified pairs.

Asteroids 69142-127502 are a second pair whose a^* colors are not the same within the estimated ± 0.1 magnitude systematic uncertainties of this survey. However, within the rather large photometric errors for these objects, the spectral profiles and a^* colors are the same (Fig. 4). The difference in filter sets used to observe this system may be the primary cause of its discrepant a^* colors. Follow-up spectroscopy could confirm or refute any taxonomic or compositional link between these objects.

The results from several other studies can be used to compare pair reflectance properties. Duddy et al. (2012) showed that the components in the pair 7343-154634 have very similar reflectance spectra. Data from Masiero et al. (2011) show that the albedos of the pair 38395-141513, as determined by observations from the Wide-field Infrared Survey Explorer mission, are nearly indistinguishable with values of 0.0638 and 0.0623 respectively. This pair was included in our sample and has a^* colors that differ by less than 0.03 magnitudes. These additional results support a compositional link between components and thus a common origin for pair systems.

449 Further comparison can be made to the survey of Ye (2011). As part of a larger
 450 sample they observed 12 asteroids in 10 pair systems with data collected for
 451 two complete pairs (1979-13732 and 11842-228747). Unfortunately the data
 452 for one component in each of the completed systems were unreliable due to
 453 instrumental problems in one case and proximity to a bright field star in the
 454 second. As such it is difficult to draw conclusions regarding the relative colors
 455 of the components in these two systems. Four of the asteroids discussed here
 456 (2110, 4765, 15107, and 54041) were also part of the Ye (2011) survey. With
 457 two exceptions the data agree within the error bars. The $V - I$ colors for
 458 15107 are significantly different: we measured $V - I = 0.77 \pm 0.06$ whereas
 459 Ye (2011) measured $V - I = 1.016 \pm 0.021$. The cause of this offset is not
 460 clear, but we note that our measured a^* colors for 15107 and its companion
 461 291188 are identical. The second discrepancy is for asteroid 4765: the data
 462 from Ye (2011) suggest $a^* = 0.06$ while SDSS MOC data suggest $a^* = -0.07$.
 463 Follow-up observations would help to clarify this inconsistency.

464 We have also shown that the a^* distribution of pairs is similar to that of all
 465 Main Belt asteroids (Fig. 7). There appears to be no bias towards a single tax-
 466 onomic complex. This strongly suggests that formation of pairs is independent
 467 of composition, and instead depends solely on the mechanical properties of the
 468 parent bodies. This is consistent with the findings of Pravec et al. (2010).

469 Taken as a whole our results are most consistent with pair formation via
 470 rotational fissioning and/or binary disruption. It is expected that a colli-
 471 sional formation between compositionally distinct bodies would produce at
 472 least some primaries and secondaries with disparate colors, though this pre-
 473 sumption should be numerically investigated in detail. It is unclear how a
 474 collisional formation scenario would influence the color distribution of pairs

475 in Figure 7. Density differences between C- and S-complex asteroids (Britt et
476 al., 2002) might be a reason for expecting different pair formation efficiencies
477 from disruptive collisions.

478 Several avenues for future work would help to further constrain the origin
479 of these objects. Spectra or photometric colors of the components in binary
480 systems could determine whether binary disruption can produce a population
481 of pairs whose primaries and secondaries have similar reflectance properties.
482 New models that address the compositional implications of pair formation via
483 rotational fission and via collisions would be useful. Additional spectroscopic
484 observations (particularly at near-infrared wavelengths) could provide further
485 insight into the composition, extent of weathering and surface properties of
486 these interesting systems.

487 **Acknowledgements**

488 I would like to thank Scott Sheppard and Mark Willman for their assis-
489 tance with observing several of the objects presented here and in their helpful
490 comments on early drafts of this manuscript. Thoughtful comments on the
491 manuscript were also provided by David Polishook. Insightful reviews were
492 kindly provided by David Vokrouhlický and an anonymous referee. This work
493 includes data obtained at the Magellan 6.5m and DuPont 2.5m telescopes lo-
494 cated at Las Campanas Observatory in Chile, and at the University of Hawaii
495 2.2m telescope located on Mauna Kea in Hawaii. Support for this project was
496 provided by the Carnegie Institution of Washington and by the National Aero-
497 nautics and Space Administration through the NASA Astrobiology Institute
498 (NAI) under Cooperative Agreement No. NNA04CC09A.

499 References

- 500 Bottke, W. F., Vokrouhlický, D., Rubincam, D. P., and Nesvorný, D., 2006.
 501 The Yarkovsky and YORP effects: Implications for asteroid dynamics. An-
 502 nual Reviews of Earth and Planetary Science 34, 157-191
- 503 Bowell, E., Hapke, B., Domingue, D., Lumme, K., Peltoniemi, J., and Harris,
 504 A., 1989. Application of photometric models to asteroids. In: Binzel, R. P.,
 505 Gehrels, T., Matthews, M. S. (Eds.), Asteroids II. Univ. Arizona Press,
 506 Tucson, pp. 524-556.
- 507 Britt, D., Yeomans, D., Housen, K., Consolmagno, G., 2002. Asteroid density,
 508 porosity and structure. In: Bottke, W. F., Cellino, A., Paolicchi, P., Binzel,
 509 R. P. (Eds.), Asteroids III. Univ. Arizona Press, Tucson, pp. 485-500.
- 510 Bus, S. J. and Binzel, R. P., 2002. Phase II of the Small Main-Belt Asteroid
 511 Spectroscopic Survey: A Feature-Based Taxonomy. Icarus 158, 146-177.
- 512 DeMeo, F. E. and 9 co-authors, 2011. A spectral comparison of (379) Huenna
 513 and its satellite. Icarus 212, 677-681.
- 514 Duddy, S. R., Lowry, S. C., Wolters, S. D., Christou, A., Weissman, P., Green,
 515 S. F., and Rozitis, B., 2012. Physical and dynamical characterisation of the
 516 unbound asteroid pair 7343-154634. A&A 539, A36.
- 517 Durda, D. D., Bottke, W. F., Nesvorný, D., Enke, B. L., Merline, W. J.,
 518 Asphaug, E., Richardson, D. C., 2007. Size-frequency distributions of frag-
 519 ments from SPH/N-body simulations of asteroid impacts: Comparison with
 520 observed asteroid families. Icarus 186, 498-516.
- 521 Ivezić, Ž. and 31 co-authors, 2001. Solar System Objects Observed in the Sloan
 522 Digital Sky Survey Commissioning Data. AJ 122, 2749-2784.
- 523 Jacobson, S. A. and Scheeres, D. J., 2011. Dynamics of rotationally fissioned
 524 asteroids: Source of observed small asteroid systems.. Icarus 214, 161-178.
- 525 Jurić, M. and 15 co-authors, 2002. Comparison of positions and magnitude of

asteroids observed in the Sloan Digital Sky Survey with those predicted for
known asteroids. AJ 124, 1776-1787.

Jester, S. and 14 co-authors, 2005. The Sloan Digital Sky Survey view of the
Palomar-Green Bright Quasar Survey. AJ 130, 873-895.

Lantz, B. and 14 co-authors, 2004. SNIFS: A wideband integral field spectro-
graph with microlens array. Proc. SPIE 5249, 146-155.

Leinhardt, Z. M. and Stewart, S. T., 2009. Full numerical simulations of catas-
trophic small body collisions. Icarus 199, 542-559.

Marchis, F. and 7 co-authors, 2008a. Main belt binary asteroidal systems with
eccentric mutual orbits. Icarus 195, 295-316.

Marchis, F. and 13 co-authors, 2008b. (3749) Balam. IAU Circ. 8928, 4.

Marchis, F., Enriquez, J. E., Emery, J. P., Berthier, J., Descamps, P., Vachier,
F., 2011. The origin of (90) Antiope from component-resolved near-infrared
spectroscopy. Icarus 213, 252-264.

Masiero, J. R. and 17 co-authors, 2011. Main Belt asteroids with
WISE/NEOWISE. I. Preliminary albedos and diameters. ApJ 741, 68-87.

Merline, W. J. and 9 co-authors, 2002. Discovery of a loosely-bound companion
to main-belt asteroids (3749) Balam. Bull. Am. Astron. Soc. 34. Abstract
02.01.

Nesvorný, D., Jedicke, R., Whiteley, R. J., and Ivezić, Ž., 2005. Evidence for
asteroid space weathering from the Sloan Digital Sky Survey. Icarus 173,
132-152.

Nesvorný, D., Enke, B. L., Bottke, W. F., Durda, D. D., Asphaug, E., and
Richardson, D. C., 2006. Karin cluster formation by asteroid impact. Icarus
183, 296-311.

Polishook, D., Brosch, N., Prialnik, D., and Kaspi, S., 2009. Simultaneous
spectroscopic and photometric observations of binary asteroids. Meteorit.

553 Planet. Sci. 44, 1955-1966.

554 Polishook, D., Brosch, N. and Prialnik, D., 2011. Rotation periods of binary
555 asteroids with large separations Confronting the Escaping Ejecta Binaries
556 model with observations. *Icarus* 212, 167-174.

557 Pravec, P. and Harris, A. W., 2000. Fast and slow rotation of asteroids. *Icarus*
558 148, 12-20.

559 Pravec, P. and Vokrouhlický, D., 2009. Significance analysis of asteroid pairs.
560 *Icarus* 204, 580-588.

561 Pravec, P., and 25 co-authors, 2010. Formation of asteroid pairs by rotational
562 fission. *Nature* 466, 1085-1088.

563 Rožek, A., Breiter, S. and Jopek, T. J., 2011. Orbital similarity functions -
564 application to asteroid pairs. *MNRAS* 412, 987-994.

565 Rubincam, D. P., 2000. Radiative spin-up and spin-down of small asteroids.
566 *Icarus* 148, 2-11.

567 Scheeres, D., 2007. Rotational fission of contact binary asteroids. *Icarus* 189,
568 370-385.

569 Scheeres, D. and Sánchez, P., 2011. Evolution of small, rapidly rotating aster-
570 oids. *Lunar Planet. Sci.* 42. Abstract No. 2307.

571 Vokrouhlický, D. and Nesvorný, D., 2008. Pairs of asteroids probably of a
572 common origin. *AJ* 136, 280-290.

573 Vokrouhlický, D. and Nesvorný, D., 2009. The common roots of asteroids
574 (6070) Rheinland and (54827) 2001 NQ8. *AJ* 137, 111-117.

575 Vokrouhlický, D., 2009. (3749) Balam: A very young multiple asteroid system.
576 *ApJ* 706, L37-L40.

577 Vokrouhlický, D. and 14 co-authors, 2011. Spin vector and shape of (6070)
578 Rheinland and their implications. *AJ* 142, 159-166.

579 Walsh, K. J., Richardson, D. C. and Michel, P., 2008. Rotational breakup as

580 the origin of small binary asteroids. *Nature* 454, 188-191.

581 Willman, M., Jedicke, R., Moskovitz, N., Nesvorný, D., Vokrouhlický, D., and
582 Mothé-Diniz, T., 2010. Using the youngest asteroid clusters to constrain
583 the space weathering and gardening rate on S-complex asteroids. *Icarus*
584 208, 758-772.

585 Ye, Q.-Z., 2011. BVRI photometry of 53 unusual asteroids. *AJ* 141, 32-39.

586 Zappalà, V., Cellino, A., Farinella, P., Milani, A., 1994. Asteroid families II.
587 Extension to unnumbered multiopposition asteroids. *AJ* 107, 772-801.

Object	UT Date	Δ (AU)	R (AU)	α (deg)
(2110) Moore-Sitterly	2010-02-28	1.661	2.513	14.2
(15107) Toepperwein	2010-02-28	1.766	2.587	14.9
(17288) 2000 NZ10	2010-03-08	2.071	2.488	22.9
(17288) 2000 NZ10	2010-08-31	1.992	2.144	27.9
(21930) 1999 VP61	2010-02-27	3.670	4.636	3.1
(22647) Levi-Strauss	2010-03-07	3.775	4.761	1.5
(32957) 1996 HX20	2010-08-31	2.044	2.330	25.6
(38395) 1999 RR193	2010-08-29	3.443	3.722	15.6
(51609) 2001 HZ32	2011-03-05	1.669	2.654	3.2
(54041) 2000 GQ113	2010-02-28	1.774	2.611	14.1
(69142) 2003 FL115	2010-08-30	1.903	2.041	29.4
(70511) 1999 TL103	2010-08-29	1.404	2.373	8.9
(84203) 2002 RD133	2010-08-29	1.069	1.850	26.3
(92652) 2000 QX36	2010-03-08	2.000	2.465	22.8
(99052) 2001 ET15	2010-03-08	1.666	2.548	12.7
(117306) 2004 VF21	2010-03-08	1.952	2.509	21.4
(127502) 2002 TP59	2012-02-14	0.928	1.888	10.1
(139537) 2001 QE25	2010-08-31	1.751	2.527	17.7
(141513) 2002 EZ93	2010-08-30	3.656	3.732	15.7
(143662) 2003 SP84	2010-02-26	1.081	1.950	18.8
(143662) 2003 SP84	2010-02-27	1.085	1.951	19.0
(189994) 2004 GH33	2010-03-07	2.059	2.390	24.3
(194083) 2001 SP159	2010-03-06	1.322	2.280	8.4
(195479) 2002 GX130	2010-03-08	1.550	2.516	6.7
(195479) 2002 GX130	2010-02-28	1.587	2.512	10.2
(203489) 2002 AL80	2010-03-07	1.905	2.608	18.1
(216177) 2006 TE23	2010-08-22	1.473	2.393	12.9
(220143) 2002 TO134	2011-03-04	1.747	2.624	12.4
(229991) 2000 AH207	2010-03-01	1.133	2.088	9.8
(237517) 2000 SP31	2010-03-06	1.798	2.709	10.3
(279865) 2001 HU24	2010-03-06	1.755	2.529	16.9
(284765) 2008 WK70	2010-03-06	1.739	2.547	15.7
(291188) 2006 AL54	2010-03-01	1.396	2.256	16.0
(291788) 2006 KM53	2010-03-07	1.628	2.581	7.6
(303284) 2004 RJ294	2010-03-08	1.334	2.086	22.4
2008 TS51	2010-03-07	1.797	2.699	10.8

Table 1: Asteroid Pairs Observed in this Study

The columns in this table are: object number and designation, UT date of observation, heliocentric distance (Δ), geocentric distance (R), and phase angle (α). Data retrieved from the Minor Planet Center website.

588

589

Object	1/2	Companion	UT Date	Instrument	V	H_V	$B - V$	$V - R$	$R - I$	a^*
(2110) Moore-Sitterly ^{bc}	1	(44612) 1999 RP27	2010-02-28	SiTe2k	17.51 ± 0.09	13.6	0.89 ± 0.02	0.45 ± 0.02	0.41 ± 0.02	0.12 ± 0.02
(15107) Toepperwein ^{ce}	1	(291188) 2006 AL54 ^b	2010-02-28	SiTe2k	18.81 ± 0.03	14.7	0.90 ± 0.07	0.45 ± 0.03	0.32 ± 0.06	0.09 ± 0.07
(17288) 2000 NZ10 ^b	1	(203489) 2002 AL80 ^b	2010-03-08	IMACS	19.03 ± 0.01	14.4	0.90 ± 0.01	0.52 ± 0.01	0.37 ± 0.01	0.11 ± 0.01
(17288) 2000 NZ10 ^b	1	(203489) 2002 AL80 ^b	2010-08-31	SiTe2k	18.86 ± 0.02	14.5	0.91 ± 0.04	0.52 ± 0.04	0.35 ± 0.05	0.11 ± 0.04
(21930) 1999 VP61 ^{ce}	1	(22647) Levi-Strauss	2010-02-27	SiTe2k	19.46 ± 0.02	13.0	0.66 ± 0.05	0.41 ± 0.04	0.36 ± 0.05	-0.11 ± 0.05
(22647) Levi-Strauss	2	(21930) 1999 VP61	2010-03-07	IMACS	19.86 ± 0.04	14.2	0.76 ± 0.06	0.42 ± 0.07	0.35 ± 0.09	-0.02 ± 0.07
(32957) 1996 HX20 ^c	2	(38707) 2000 QK89	2010-08-31	SiTe2k	20.66 ± 0.04	16.1	0.86 ± 0.05	0.52 ± 0.03	0.21 ± 0.06	0.02 ± 0.05
(38395) 1999 RR193	1	(141513) 2002 EZ93	2010-08-29	SiTe2k	20.13 ± 0.04	13.7	0.71 ± 0.05	0.39 ± 0.07	0.39 ± 0.10	-0.05 ± 0.06
(51609) 2001 HZ32 ^{ce}	1	1999 TE221 ^b	2011-03-05	IMACS	19.12 ± 0.06	15.6	0.82 ± 0.04	0.38 ± 0.04	0.35 ± 0.07	0.03 ± 0.05
(54041) 2000 GQ113 ^{bce}	1	(220143) 2002 TO134	2010-02-28	SiTe2k	19.04 ± 0.02	14.9	0.85 ± 0.08	0.50 ± 0.06	0.23 ± 0.02	0.01 ± 0.07
(69142) 2003 FL115 ^c	1	(127502) 2002 TP59	2010-08-30	SiTe2k	20.08 ± 0.19	15.9	0.88 ± 0.13	0.44 ± 0.02	0.49 ± 0.07	0.15 ± 0.12
(70511) 1999 TL103 ^{ce}	1	2007 TC334	2010-08-29	SiTe2k	18.71 ± 0.04	15.5	0.93 ± 0.05	0.54 ± 0.03	0.09 ± 0.05	0.03 ± 0.05
(84203) 2002 RD133 ^c	1	(285637) 2000 SS4	2010-08-29	SiTe2k	19.27 ± 0.07	16.6	0.67 ± 0.04	0.41 ± 0.04	0.41 ± 0.05	-0.08 ± 0.04
(92652) 2000 QX36	1	(194083) 2001 SP159	2010-03-08	IMACS	20.42 ± 0.01	15.9	0.88 ± 0.02	0.50 ± 0.01	0.39 ± 0.01	0.10 ± 0.02
(99052) 2001 ET15 ^{ae}	1	(291788) 2006 KM53	2010-03-08	IMACS	19.47 ± 0.01	15.6	0.87 ± 0.01	0.48 ± 0.01	0.45 ± 0.01	0.12 ± 0.02
(117306) 2004 VF21	2	(10123) Figeoja ^a	2010-03-08	IMACS	20.91 ± 0.01	16.4	0.87 ± 0.03	0.53 ± 0.01	-	-
(139537) 2001 QE25 ^c	1	(210904) 2001 SR218	2010-08-31	SiTe2k	19.51 ± 0.04	15.4	0.67 ± 0.03	0.43 ± 0.03	0.32 ± 0.06	-0.11 ± 0.04
(141513) 2002 EZ93 ^c	2	(38395) 1999 RR193	2010-08-30	SiTe2k	21.12 ± 0.10	14.6	0.68 ± 0.04	0.36 ± 0.05	0.40 ± 0.08	-0.07 ± 0.05
(143662) 2003 SP84 ^c	2	(92336) 2000 GY81	2010-02-26	SiTe2k	19.51 ± 0.13	16.9	0.88 ± 0.07	0.48 ± 0.03	0.39 ± 0.04	0.10 ± 0.07
(143662) 2003 SP84	2	(92336) 2000 GY81	2010-02-27	SiTe2k	19.45 ± 0.04	16.9	0.82 ± 0.07	0.42 ± 0.04	0.47 ± 0.06	0.09 ± 0.06
(189994) 2004 GH33	1	(303284) 2004 RJ294	2010-03-07	IMACS	21.93 ± 0.05	17.3	0.89 ± 0.09	0.49 ± 0.08	0.36 ± 0.10	0.10 ± 0.09
(194083) 2001 SP159	2	(92652) 2000 QX36	2010-03-06	IMACS	20.05 ± 0.05	17.1	0.84 ± 0.07	0.50 ± 0.07	0.43 ± 0.08	0.08 ± 0.07
(195479) 2002 GX130 ^e	1	(284765) 2008 WK70	2010-03-08	IMACS	19.90 ± 0.01	16.4	0.88 ± 0.02	0.51 ± 0.01	0.30 ± 0.01	0.06 ± 0.02
(195479) 2002 GX130 ^c	1	(284765) 2008 WK70	2010-02-28	SiTe2k	20.12 ± 0.07	16.5	0.87 ± 0.08	0.43 ± 0.03	0.35 ± 0.03	0.07 ± 0.08
(203489) 2002 AL80 ^b	2	(17288) 2000 NZ10 ^b	2010-03-07	IMACS	21.00 ± 0.04	16.6	0.93 ± 0.07	0.50 ± 0.07	0.36 ± 0.09	0.13 ± 0.08
(216177) 2006 TE23 ^{cde}	2	(34380) 2000 RV55 ^b	2010-08-22	IMACS	20.20 ± 0.07	16.7	0.81 ± 0.05	0.46 ± 0.02	0.33 ± 0.04	0.02 ± 0.04

(220143)	2002 TO134^{ce}	2	(54041)	2000 GQ113 ^b	2011-03-04	IMACS	20.87 ± 0.07	16.8	0.86 ± 0.07	0.52 ± 0.05	0.28 ± 0.08	0.04 ± 0.07
(229991)	2000 AH207 ^c	2	(106598)	2000 WZ112	2010-03-01	SITe2k	19.65 ± 0.04	17.1	0.86 ± 0.13	0.41 ± 0.06	0.30 ± 0.05	0.05 ± 0.12
(237517)	2000 SP31	1	2007	TN127	2010-03-06	IMACS	22.22 ± 0.06	18.1	0.84 ± 0.12	0.32 ± 0.08	0.25 ± 0.09	0.01 ± 0.11
(279865)	2001 HU24	2	(52773)	1998 QU12	2010-03-06	IMACS	21.78 ± 0.05	17.6	0.88 ± 0.08	0.46 ± 0.07	0.44 ± 0.09	0.12 ± 0.08
(284765)	2008 WK70	2	(195479)	2002 GX130	2010-03-06	IMACS	21.34 ± 0.05	17.3	0.78 ± 0.09	0.45 ± 0.07	0.42 ± 0.09	0.02 ± 0.09
(291188)	2006 AL54^{bc}	2	(15107)	Toepferwein	2010-03-01	SITe2k	20.70 ± 0.08	17.3	0.86 ± 0.15	0.51 ± 0.07	0.41 ± 0.06	0.10 ± 0.14
(291788)	2006 KM53	2	(99052)	2001 ET15 ^a	2010-03-07	IMACS	20.23 ± 0.04	16.6	0.82 ± 0.06	0.48 ± 0.07	0.37 ± 0.09	0.04 ± 0.07
(303284)	2004 RJ294^b	2	(189994)	2004 GH33	2010-03-08	IMACS	21.33 ± 0.02	18.0	0.90 ± 0.04	0.54 ± 0.02	0.40 ± 0.01	0.12 ± 0.04
2008 TS51		2	2002	RJ126	2010-03-07	IMACS	22.49 ± 0.06	18.4	0.66 ± 0.11	0.29 ± 0.08	0.28 ± 0.11	-0.14 ± 0.11

Table 2: Summary of Asteroid Pair *BVRI* observations

The columns in this table are: object number and designation, pair primary (1) or secondary (2), companion number and designation, UT date of observation, instrument employed, measured *V*-band magnitude, calculated absolute *V*-band magnitude at zero phase angle (see text), and photometric colors. Entries in bold indicate pairs where data was obtained or already exists for both components.

^a Observed spectroscopically.

^b Observed by SDSS.

^c Multiple *BVRI* sequences. The *V*-band error represents the standard deviation of all measured *V*-band magnitudes.

^d Spurious pair.

^e Photometry calibrated with SDSS field stars.

Object	1/2	Companion	r	$u - g$	$g - r$	$r - i$	$i - z$	a^*
(2110) Moore-Sitterly ^a	1	(44612) 1999 RP27	14.88 ± 0.03	1.73 ± 0.06	0.67 ± 0.04	0.28 ± 0.04	-0.05 ± 0.03	0.15 ± 0.04
(4765) Wasserburg	1	2001 XO105	16.46 ± 0.02	1.41 ± 0.04	0.49 ± 0.04	0.15 ± 0.02	0.05 ± 0.02	-0.07 ± 0.04
(10484) Hecht	1	(44645) 1999 RC118	17.07 ± 0.01	1.76 ± 0.03	0.39 ± 0.01	0.20 ± 0.01	-0.26 ± 0.02	0.16 ± 0.01
(17288) 2000 NZ10^a	1	(203489) 2002 AL80 ^a	17.87 ± 0.01	1.66 ± 0.16	0.68 ± 0.02	0.17 ± 0.02	-0.01 ± 0.03	0.11 ± 0.02
(34380) 2000 RV55^c	1	(216177) 2006 TE23 ^a	19.60 ± 0.02	1.71 ± 0.27	0.72 ± 0.04	0.24 ± 0.04	-0.07 ± 0.06	0.18 ± 0.04
(38184) 1999 KF	1	(221867) 2008 GR90	18.77 ± 0.02	1.70 ± 0.12	0.70 ± 0.03	0.18 ± 0.03	-0.01 ± 0.04	0.13 ± 0.03
(54041) 2000 GQ113^a	1	(220143) 2002 TO134 ^a	18.27 ± 0.02	1.58 ± 0.06	0.63 ± 0.04	0.20 ± 0.03	-0.20 ± 0.03	0.08 ± 0.04
(63440) 2001 MD30	1	2004 TV14	17.10 ± 0.01	1.29 ± 0.07	0.52 ± 0.02	0.17 ± 0.01	0.02 ± 0.15	-0.03 ± 0.02
(106700) 2000 WX167	1	(263114) 2007 UV	19.07 ± 0.02	1.36 ± 0.08	0.59 ± 0.03	0.15 ± 0.03	0.08 ± 0.04	0.02 ± 0.03
(113029) Priscus	1	(113029) 2002 RZ46	19.93 ± 0.02	1.07 ± 0.30	0.69 ± 0.04	0.26 ± 0.04	-0.05 ± 0.08	0.16 ± 0.04
(127502) 2002 TP59^b	2	(69142) 2003 FL115 ^a	18.76 ± 0.10	-	0.57 ± 0.15	0.22 ± 0.11	-	0.04 ± 0.14
(203489) 2002 AL80^a	2	(17288) 2000 NZ10 ^a	20.02 ± 0.02	1.06 ± 0.30	0.65 ± 0.04	0.19 ± 0.04	-0.04 ± 0.08	0.09 ± 0.04
(250322) 2003 SC7	2	(52852) 1998 RB75	19.91 ± 0.02	0.87 ± 0.35	0.58 ± 0.04	0.19 ± 0.04	-0.10 ± 0.09	0.03 ± 0.04
(291188) 2006 AL54^a	2	(15107) Toepperwein ^a	19.88 ± 0.02	1.39 ± 0.20	0.67 ± 0.04	0.20 ± 0.03	0.00 ± 0.06	0.11 ± 0.04
(303284) 2004 RJ294^a	2	(189994) 2004 GH33 ^a	21.09 ± 0.05	1.45 ± 0.54	0.69 ± 0.08	0.16 ± 0.07	-0.10 ± 0.20	0.12 ± 0.08
1999 TE221	2	(51609) 2001 HZ32 ^a	18.66 ± 0.02	1.46 ± 0.08	0.55 ± 0.03	0.20 ± 0.03	-0.32 ± 0.04	0.01 ± 0.03
2003 YK39	2	(21436) Chaoyichi	19.82 ± 0.03	1.92 ± 0.31	0.75 ± 0.04	0.06 ± 0.04	-0.07 ± 0.07	0.12 ± 0.04

Table 3: Summary of Asteroid Pair *ugriz* data

In all but one case, (127502) 2002 TP59, these data were retrieved from the SDSS MOC. The columns in this table are: object number and designation, pair primary (1) or secondary (2), companion number and designation, *r*-band magnitude, and photometric colors. Entries in bold indicate pairs where data was obtained for both components.

^a BVRI observations were performed.

^b Observed with SNIFS at the University of Hawaii 2.2m telescope on UT 14 February, 2012. Multiple *gri* sequences were obtained. The phase corrected absolute magnitude for this object is $H_r=16.9$ (see text).

^c Spurious pair.

Object	UT Date	Mag.	t_{exp} (s)	Solar Analog	Taxon
(10123) Figeoja	2010-03-06	17.7	600	SA104-335	Ld
(99052) 2001 ET15	2010-03-08	19.47	600	HD127913	S

Table 4

IMACS spectroscopic observations

591

592

Primary	Secondary	Primary a^*	Secondary a^*	Taxonomic Complex
(15107) Toepperwein	(291188) 2006 AL54	0.09 ± 0.07	0.09 ± 0.14	S
(17288) 2000 NZ10	(203489) 2002 AL80	0.11 ± 0.01	0.13 ± 0.08	S
(21930) 1999 VP61	(22647) Levi-Strauss	-0.11 ± 0.05	-0.02 ± 0.07	C
(38395) 1999 RR193	(141513) 2002 EZ93	-0.05 ± 0.06	-0.07 ± 0.05	C
(51609) 2001 HZ32	1999 TE221	0.03 ± 0.05	0.01 ± 0.03	S
(54041) 2000 GQ113	(220143) 2002 TO134	0.01 ± 0.07	0.04 ± 0.07	S
(69142) 2003 FL115	(127502) 2002 TP59	0.15 ± 0.12	0.04 ± 0.14	S
(92652) 2000 QX36	(194083) 2001 SP159	0.10 ± 0.02	0.08 ± 0.07	S
(99052) 2001 ET15	(291788) 2006 KM53	0.12 ± 0.01	0.04 ± 0.07	S
(189994) 2004 GH33	(303284) 2004 RJ294	0.10 ± 0.09	0.12 ± 0.04	S
(195479) 2002 GX130	(284765) 2008 WK70	0.06 ± 0.02	0.02 ± 0.05	S

Table 5

Comparison of Primary and Secondary a^* Colors

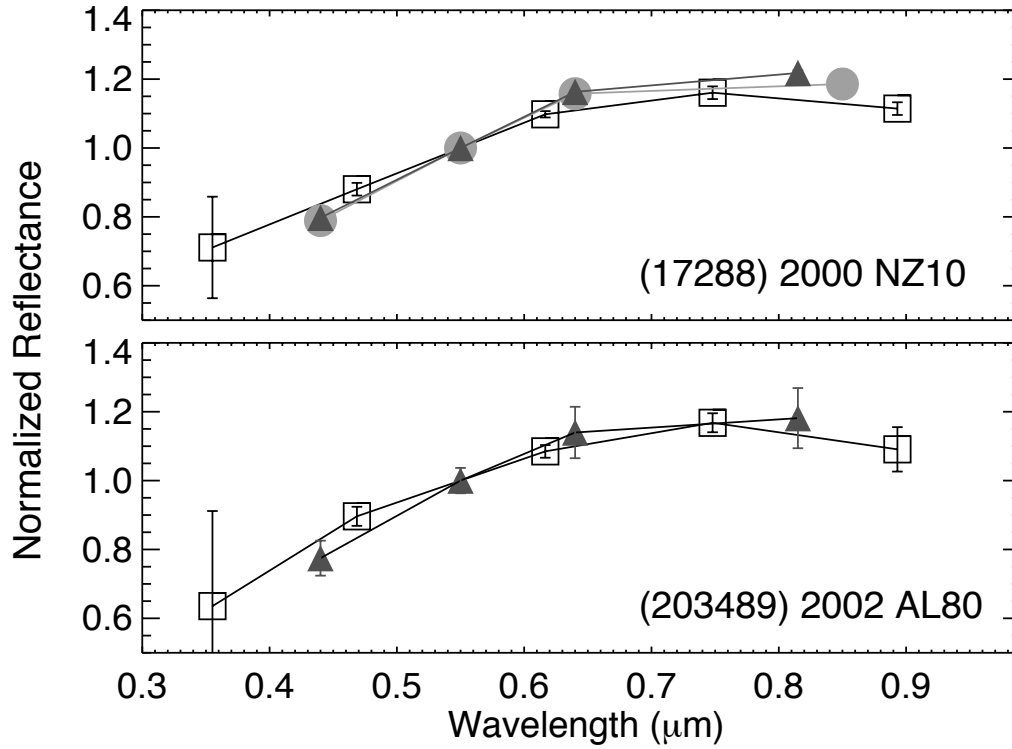


Fig. 1. Spectro-photometry of asteroid pair primary 17288 (top) and secondary 203489 (bottom). SDSS *ugriz* photometry is shown as open squares. *BVRI* photometry from IMACS/Magellan is shown as dark grey triangles and from DuPont as light grey circles. Some error bars fall within the size of the symbols. The data are normalized at 0.55 microns. The repeat observations of each object are highly consistent. The reflectance profiles of these two objects are very similar.

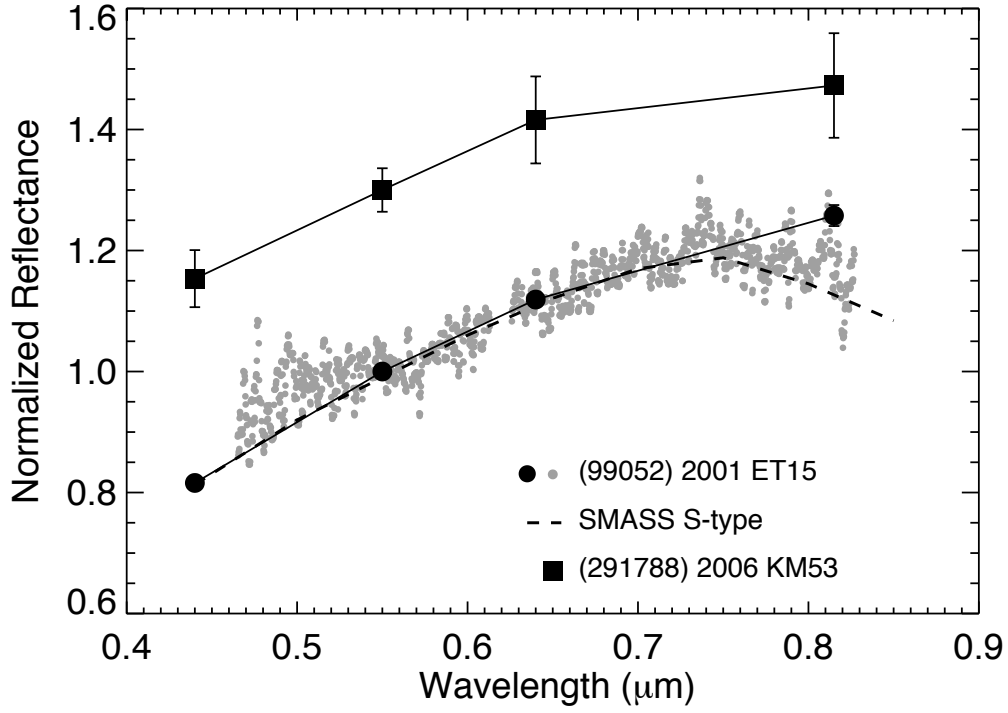


Fig. 2. Reflectance measurements of pair 99052-291788. *BVRI* photometry and a spectrum were measured for the primary 99052. The two different techniques produced very similar results. The spectrum is best fit by an S-type in the SMASS taxonomic system (dashed). The data for the secondary 291788 are vertically offset by 0.3 units and closely match the spectro-photometry of 99052.

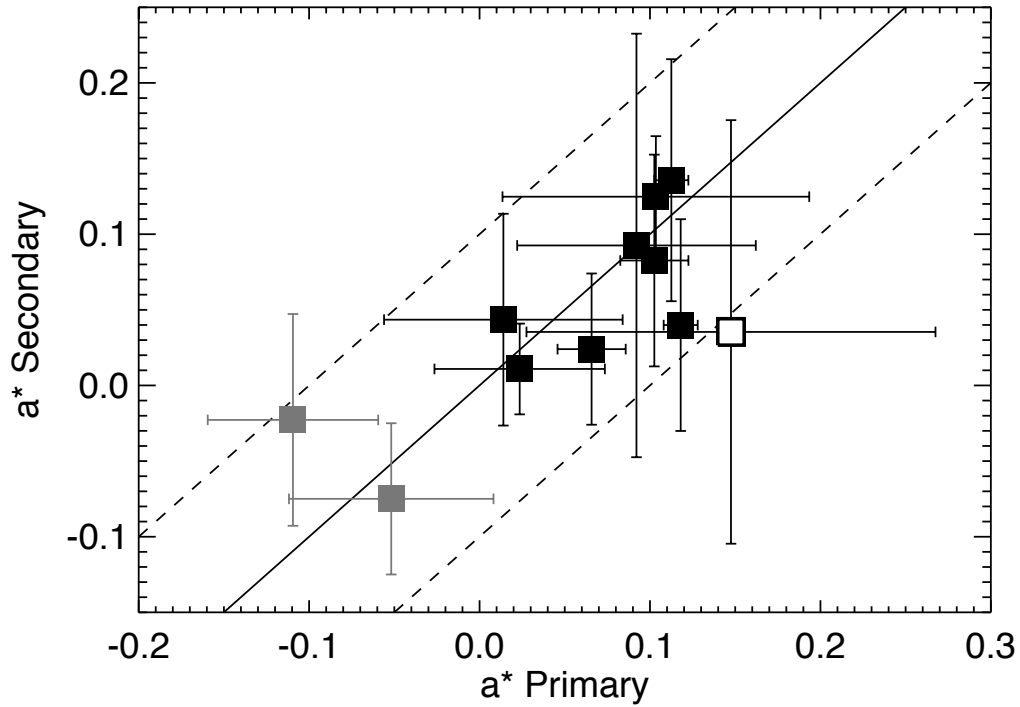


Fig. 3. Comparison of a^* colors for the primary and secondary components in 11 pair systems. The solid line has a slope of one, representing a perfect match of primary and secondary colors. The dashed lines represent estimates on the systematic uncertainties (± 0.1) of our observations. The grey symbols indicate a^* colors consistent with the C- taxonomic complex ($a^* < 0.0$), the black symbols indicate colors consistent with the S-complex ($a^* > 0.0$). The open symbol is the only pair that falls outside of our systematic uncertainties. This distribution of colors is non-random at a significance level of $>98\%$.

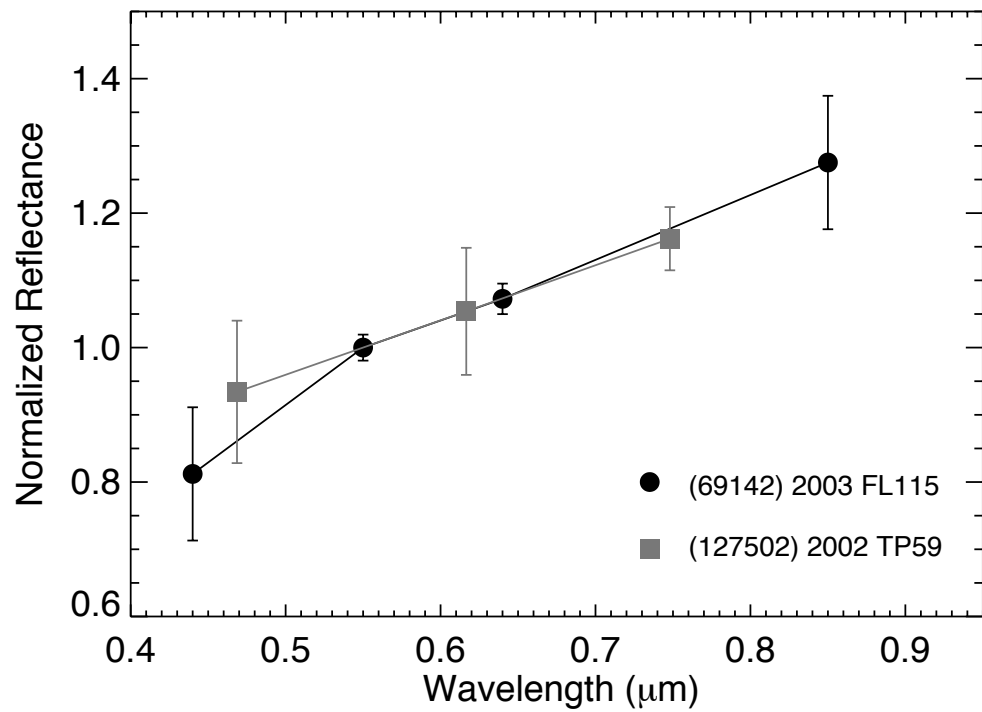


Fig. 4. Photometry of asteroid pair 69142 (*BVRI*) and 127502 (*gri*). Though the a^* colors of these asteroids differ by more than 0.1 magnitudes, they are the same within the errors bars.

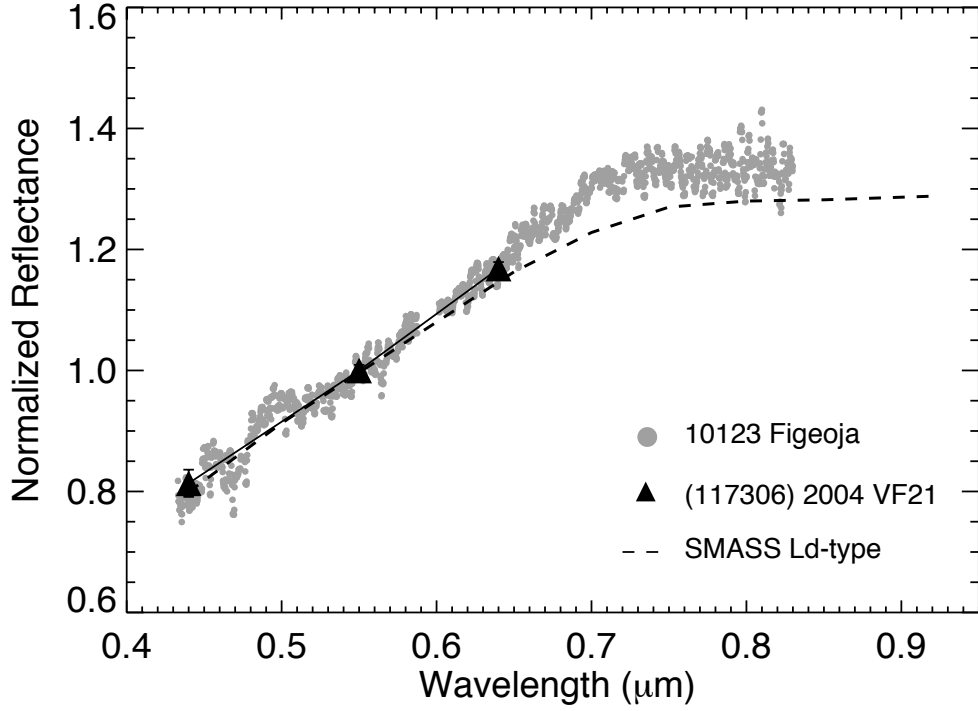


Fig. 5. Observations of asteroid pair 10123-117306. The IMACS spectrum of 10123 (grey dots) is indicative of an SMASS Ld-type (dashed line). The photometric error bars for 117306 mostly fall within the size of the symbols. Only *BVR* images were obtained for the secondary 117306 because of interference by a background field star during the *I*-band exposure. Nevertheless the spectral profiles of these objects are very similar.

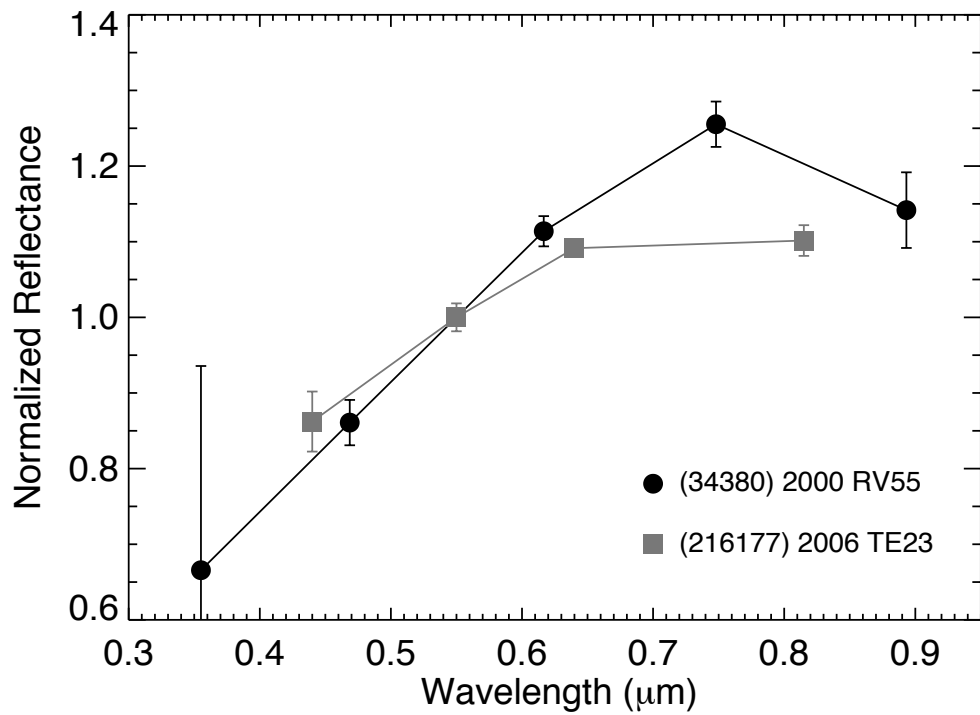


Fig. 6. Photometry of reported asteroid pair 34380 (SDSS *ugriz*) and 216177 (*BVRi*). Though originally identified as a pair with a low probability of association (Pravec et al., 2010), updated dynamical integrations suggest that this pair is actually spurious.

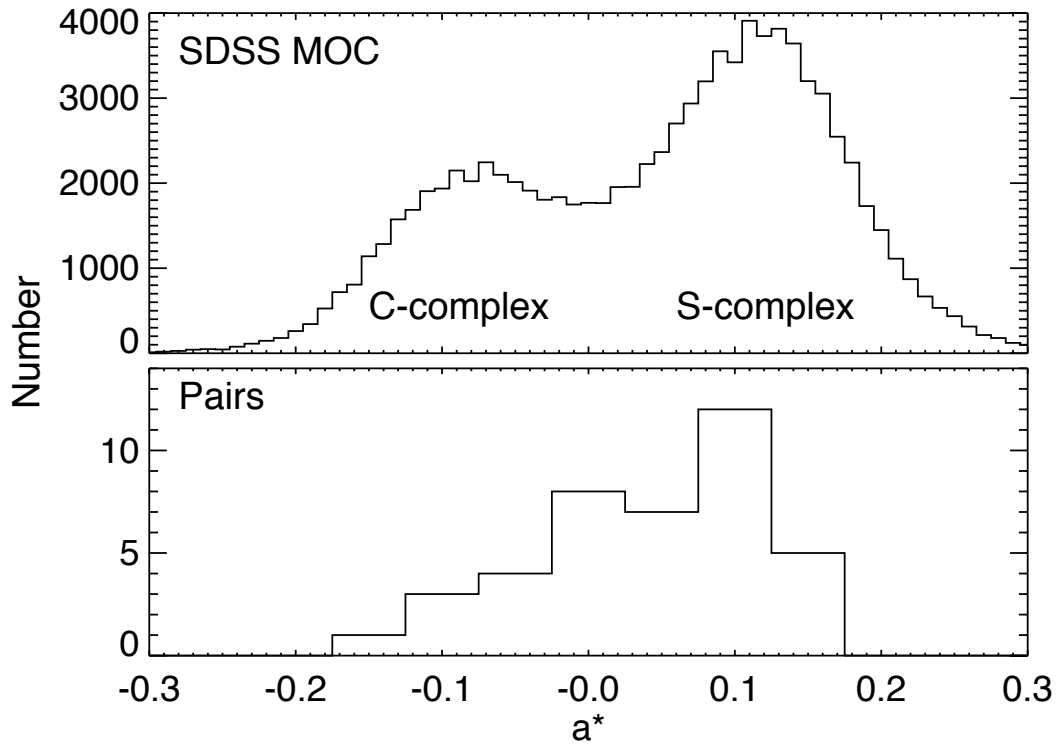


Fig. 7. Histograms of a^* values for all objects within the SDSS MOC (top) and for all pairs considered in this study (bottom). The apparent bi-modality is attributed to the color difference between C- and S-complex asteroids. There is no statistically significant difference between these two distributions, suggesting that pairs represent an unbiased cross section of the compositional diversity of asteroids within the Main Belt.